Supporting Information: Quasinormal Coupled-Mode Analysis of Dynamic Gain in Exceptional-Point Lasers

Hao He,[*,†] Xingwei Gao,[†] Alexander Cerjan,[*,‡] and Chia Wei Hsu[†]

†*Ming Hsieh Department of Electrical and Computer Engineering, University of Southern California, Los Angeles, CA 90089, USA*

‡*Center for Integrated Nanotechnologies, Sandia National Laboratories, Albuquerque, NM 87185, USA*

E-mail: hehao@usc.edu; awcerja@sandia.gov

S1: Quasinormal mode and quasinormal expansion in 1D

In this section, we first introduce the concept of QNM and its corresponding properties in 1D systems, then derive the QNM expansion equation Eq. (4) in the main text.

For a 1D resonator in free space environment, QNMs are defined as the solution to source-free eigenvalue problem

$$\frac{d^2\tilde{E}_m(x)}{dx^2} + \left(\frac{\tilde{\omega}_m}{c}\right)^2 \varepsilon_r(x)\,\tilde{E}_m(x) = 0, \tag{S1}$$

with outgoing boundary condition $\tilde{E}_m(x = x_{1,2}) \propto e^{\mp i(\tilde{\omega}_m/c)x}$, where $\{x_1, x_2\}$ are two arbitrary points in the uniform environment.

Due to the radiation loss and material absorption, all QNM frequencies in this resonator should have negative imaginary part. The interplay of outgoing boundary condition and the negative imaginary part leads to an exponentially diverging tail of the QNM field outside the resonator. Therefore, QNM profiles extend to infinity and are intrinsically not square-integrable.

Instead of integrating the wave function in the infinite space, it is possible to integrate the wave function within a finite region enclosed by the two points $x = x_{1,2}$ in the surrounding free space. Multiply Eq. (S1) by $\tilde{E}_{n(x)}$ then integrate over region $[x_1, x_2]$, we get

$$\int_{x_1}^{x_2} \left[\tilde{E}_n(x) \frac{d^2 \tilde{E}_m(x)}{dx^2} + \frac{\tilde{\omega}_m^2}{c^2} \varepsilon_r(x) \tilde{E}_n(x) \tilde{E}_m(x) \right] dx = 0. \tag{S2}$$

Integrating by parts, Eq. (S2) can be written as

$$\left[\tilde{E}_n(x) \frac{d\tilde{E}_m(x)}{dx} - \tilde{E}_m(x) \frac{d\tilde{E}_n(x)}{dx} \right]_{x_1}^{x_2} + \int_{x_1}^{x_2} \tilde{E}_m(x) \frac{d^2 \tilde{E}_n(x)}{dx^2} dx + \frac{\tilde{\omega}_m^2}{c^2} \int_{x_1}^{x_2} \varepsilon_r \tilde{E}_n(x) \tilde{E}_m(x) dx = 0. \tag{S3}$$

Subtracting $\int_{x_1}^{x_2} dx\, \tilde{E}_m(x) \cdot$ Eq. (S1) with $m \to n$, then substituting the first derivative using the outgoing boundary condition $\frac{d\tilde{E}_m(x_{1,2})}{dx} = \mp i \frac{\tilde{\omega}_m}{c} \tilde{E}_m(x_{1,2})$, we obtain the orthogonality relation,

$$(\tilde{\omega}_m - \tilde{\omega}_n) \left[i \frac{\tilde{E}_m(x_1) \tilde{E}_n(x_1) + \tilde{E}_m(x_2) \tilde{E}_n(x_2)}{(\tilde{\omega}_m + \tilde{\omega}_n)/c} + \int_{x_1}^{x_2} \varepsilon_r \tilde{E}_n(x) \tilde{E}_m(x) dx \right] = 0. \tag{S4}$$

The term in the bracket is defined as the regularized inner product $\langle \tilde{E}_n | \tilde{E}_m \rangle$. Obviously, in non-degenerate systems, $\langle \tilde{E}_n | \tilde{E}_m \rangle = 0$ for $n \neq m$ and $\langle \tilde{E}_n | \tilde{E}_m \rangle$ can be nonzero only when $n = m$, which defines the normalization of $\tilde{E}_m$.

It is worth noting that, although orthogonality relation Eq. (S4) is derived by integrating from x_1 to x_2, such defined inner product is unique and independent of the choice of $\{x_1, x_2\}$, so long as $\{x_1, x_2\}$ are both chosen in the uniform environment medium. The proof is straightforward as the change in the surface term caused by different choice of $\{x_1', x_2'\}$

cancels the change in the volume integral. Therefore, this inner product is unique and carries physical significance for the QNMs.

With the inner product defined above, consider a harmonic polarization density $P(x,t) = P(x)\,e^{-i\omega t}$ as the source to excite the resonator. The excited field $E(x,t)$ is determined by

$$\frac{\partial^2 E(x,t)}{\partial x^2} - \varepsilon_r(x)\frac{1}{c^2}\frac{\partial^2 E(x,t)}{\partial t^2} = \frac{1}{c^2}\frac{\partial^2 \left[P(x)\,e^{-i\omega t}\right]}{\partial t^2}. \tag{S5}$$

Expanding the electric field onto the QNM basis as $E(x,t) = \sum_n A_n(t)\,E_n(x)\,e^{-i\tilde{\omega}_n t}$, where $A_n(t)$ is the time-dependent amplitude of QNM $\tilde{E}_n$. Substitute it back into Eq. (S5), we obtain

$$\sum_n -\varepsilon_r \tilde{E}_n(x)\frac{1}{c^2}\left(\frac{d^2 A_n}{dt^2} - 2i\tilde{\omega}_n\frac{dA_n}{dt}\right)e^{-i\tilde{\omega}_n t} = -\frac{\omega^2}{c^2}P(x)\,e^{-i\omega t}. \tag{S6}$$

For near resonance excitation $|\omega - \tilde{\omega}_m| \ll |\omega|$, the second derivative terms on the left side is small relative to the first derivatives and thus can be ignored. This is known as the slowly-varying envelope approximation (SVEA). By taking the inner product of both sides with $\tilde{E}_m$, we obtain

$$\frac{dA_m(t)}{dt} = -\frac{\omega^2\left[\int_{x_1}^{x_2}\tilde{E}_m(x)\,P(x)\,dx\right]}{2i\tilde{\omega}_m\langle\tilde{E}_m|\tilde{E}_m\rangle}e^{-i(\omega-\tilde{\omega}_m)t}. \tag{S7}$$

Here, $P(x)$ is assumed to be zero outside the resonator structure. After a gauge transform: $a_m(t) = A_m(t)\,e^{-i\tilde{\omega}_m t}$, the QNM expansion equations take the form of typical TCMT,

$$\frac{da_m(t)}{dt} = -i\tilde{\omega}_m a_m(t) - \frac{\omega^2\left[\int_{x_1}^{x_2}\tilde{E}_m(x)\,P(x)\,dx\right]}{2i\tilde{\omega}_m\langle\tilde{E}_m|\tilde{E}_m\rangle}e^{-i\omega t}. \tag{S8}$$

At steady state, the field would synchronize with the harmonic source and oscillate at the same frequency: $a_m(t) = a_m e^{-i\omega t}$. The steady state amplitude of QNM $\tilde{E}_m$ is thus given by

$$a_m = \frac{\omega^2\left[\int_{x_1}^{x_2}\tilde{E}_m(x)\,P(x)\,dx\right]}{2\tilde{\omega}_m\left(\tilde{\omega}_m - \omega\right)\langle\tilde{E}_m|\tilde{E}_m\rangle}. \tag{S9}$$

Or if SVEA not adopted

$$a_m = \frac{\omega^2 \left[\int_{x_1}^{x_2} \tilde{E}_m(x) P(x) dx\right]}{(\tilde{\omega}_m^2 - \omega^2) \langle \tilde{E}_m | \tilde{E}_m \rangle}. \tag{S10}$$

Similar to the 1D case discussed above, QNMs in 3D are also defined as the eigensolution of the source-free Maxwell equations with outgoing boundary conditions. The corresponding inner product in 3D can be obtained from the unconjugated form of the Lorentz reciprocity theorem.[S1] In practice, outgoing boundary conditions are usually implemented with perfectly matched layers (PMLs), which can damp out the exponential growth of QNMs away from the resonator and make QNMs square-integrable.[S2] The vanishing field at the outer surface of PMLs leads to a zero surface integral in the unconjugated Lorentz reciprocity theorem, and thus defines a complete and orthogonal basis formed by QNMs. The orthogonal inner product defined with PMLs suffices to determine the expansion coefficients, but might have slightly different form compared with other derivations due the the overcompleteness of QNMs.[S1,S3,S4]

S2: QNM expansion: below first lasing threshold

In the following sections, the QNM expansion formalism is applied to the PALT theory. Here we consider the same 1D coupled-cavity resonator structure described in the main text.

When the active medium is pumped at a relatively small pumping strength $D_{\max}$, the pump-induced polarization density $P(x) = \Gamma_\perp(\omega) D_{\mathrm{P}}(x) E(x)$ can be treated as an external driving source. Here $\Gamma_\perp(\omega) = \gamma_\perp / (\omega - \omega_{ab} + i\gamma_\perp)$ is the dispersive gain curve. $D_{\mathrm{P}}(x) = D_{\max} \mathrm{Win}(x)$ is the pump distribution, $D_{\max}$ is the pumping strength and $\mathrm{Win}(x)$ is the fixed pump profile. Since the excited amplitudes Eq. (S10) have a dispersive contribution which is maximized when the frequency difference is small, considering the contribution from the two modes near the gain center is sufficient to model this lasing behavior. So, the electric field can be expanded onto this 2-QNM basis as $E(x) \approx a\tilde{E}_a(x) + b\tilde{E}_b(x)$ and $\{a, b\}$ are the constant QNM amplitudes.

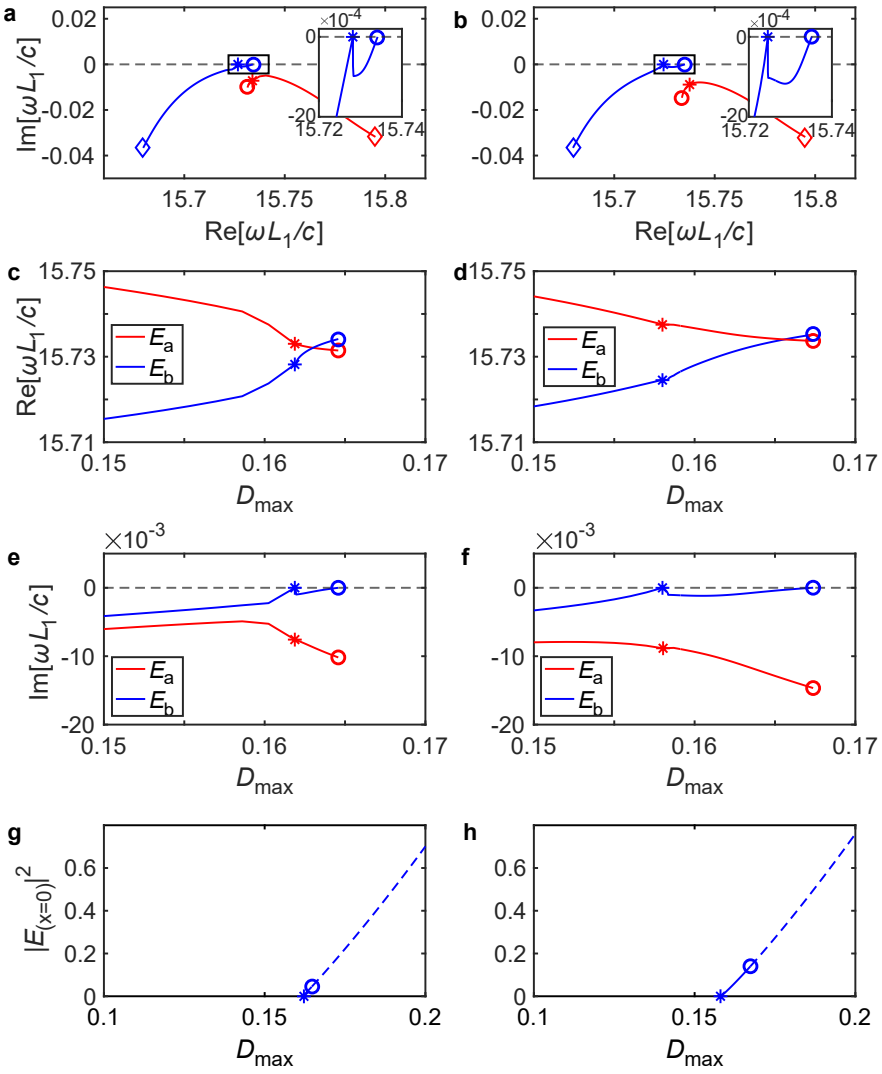

Figure S1: The left column is the exact result from Green's function, and the right column is the result from QNM expansion. **a-b**, The trajectory of the complex perturbation frequency as pumping strength $D_{\max}$ increases. The inset shows a zoom-in plot of the boxed area. **c-f**, The evolution of complex perturbation frequency as a function of pumping strength $D_{\max}$. The square, star, and circle represent $D_{\max} = 0$, $D_{\max} = D_1^{th}$, $D_{\max} = D_c^{th}$, respectively. $D_1^{th} = 0.1619, D_c^{th} = 0.1646$ for Green's function result and $D_1^{th} = 0.1580, D_c^{th} = 0.1674$ for QNM expansion result. **g-h**, Single-mode lasing intensity as a function of pumping strength $D_{\max}$. Dashed lines correspond to unstable solutions.

Under the QNM expansion, the wave equation with $P(x) = \Gamma_\perp(\omega) D_{\mathrm{P}}(x) E(x)$ as a source can be written as

$$\left(\tilde{\omega}_a^2 - \omega^2\right) a\langle \tilde{E}_a | \tilde{E}_a \rangle = \omega^2 \Gamma_\perp(\omega) D_{\max} \left[\left(\int_{x_1}^{x_2} \mathrm{Win}(x) \tilde{E}_a(x)^2 dx \right) a + \left(\int_{x_1}^{x_2} \mathrm{Win}(x) \tilde{E}_a(x) \tilde{E}_b(x) dx \right) b \right], \tag{S11}$$

$$\left(\tilde{\omega}_b^2 - \omega^2\right) b\langle \tilde{E}_b | \tilde{E}_b \rangle = \omega^2 \Gamma_\perp(\omega) D_{\max} \left[\left(\int_{x_1}^{x_2} \mathrm{Win}(x) \tilde{E}_b(x)^2 dx \right) b + \left(\int_{x_1}^{x_2} \mathrm{Win}(x) \tilde{E}_b(x) \tilde{E}_a(x) dx \right) a \right], \tag{S12}$$

which are just linear homogeneous equations of $\{a, b\}$. The field integrals are constant independent of $\{a, b\}$ and $D_{\max}$, so one can numerically calculate them with precomputed QNM field profiles $\tilde{E}_{a,b}(x)$. Finding a non-zero solution to Eq. (S11)-(S12) requires a vanishing determinant of the coefficient matrix. Numerically solving this equation of vanishing determinant gives possible solutions of complex frequency ω, which is plotted in Fig. S1**b**. Increasing pumping strength $D_{\max}$ is equivalent to increase gain in this case.

Although the complex frequencies move toward the real axis as the pumping strength increases, they cannot go beyond the real axis as this would otherwise result in unphysical diverging field. The critical point is when one of those complex frequencies first reaches the real axis, which marks the onset of the single-mode lasing. The pumping strength at this point is labeled as the first lasing threshold $D_{\max} = D_1^{th}$.

S3: QNM expansion: single-mode lasing and stability analysis

In the main text, the single-mode lasing is analyzed in a single cavity edge emitting laser, where only one QNM dominates the passive cavity response. In this section, we consider the single-mode lasing in the coupled-cavity structure shown in Fig. 3, where both the two QNMs contribute to the single-mode lasing simultaneously. The QNM expansion equations

for single-mode lasing and its PALT stability analysis are derived.

Beyond the first lasing threshold, the pump-induced gain balances the intrinsic loss of QNM and leads to stable single-mode lasing. Since the loss of the QNM is solely determined by $-\mathrm{Im}\left(\tilde{\omega}_n\right)$, the complete gain-loss cancellation requires the gain to remain constant while the pumping strength increases. This resistive mechanism in gain-pump relation is known as the gain saturation and can be expressed as a saturated polarization density

$$\frac{d^2E_0\left(x\right)}{dx^2}+\left(\frac{\omega_0}{c}\right)^2\varepsilon_r\left(x\right)E_0\left(x\right)=-\left(\frac{\omega_0}{c}\right)^2\frac{\Gamma_0 D_{\mathrm{P}}\left(x\right)}{1+|\Gamma_0|^2|E_0\left(x\right)|^2}E_0\left(x\right), \tag{S13}$$

where $\Gamma_0=\Gamma_\perp\left(\omega_0\right)$. Under the QNM expansion, the field is projected onto the 2-QNM basis as $E_0\left(x\right)=a_0\tilde{E}_a\left(x\right)+b_0\tilde{E}_b\left(x\right)$. Observing that $P\left(x\right)$ is nonzero only inside the pumped cavity, it is fair to assume that the two QNMs share the same field profile $E_\alpha\left(x\right)$ inside the pumped cavity

$$\tilde{E}_{a,b}\left(x\right)=\alpha_{1,2}E_\alpha\left(x\right), \quad \text{for } x\in \mathrm{C_{act}}, \tag{S14}$$

as plotted in Fig. 3**d** & **e**. This assumption is guaranteed by the weak spatial coupling limit in such EP-laser.[S5] As a result, the QNM amplitude equations for the single-mode lasing operation can be simplified as

$$\left(\tilde{\omega}_a^2-\omega_0^2\right)a_0\langle\tilde{E}_a|\tilde{E}_a\rangle=\omega_0^2\Gamma_0 D_{\max}\alpha_1\left(a_0\alpha_1+b_0\alpha_2\right)F\left(|\Gamma_0|^2|a_0\alpha_1+b_0\alpha_2|^2\right), \tag{S15}$$

$$\left(\tilde{\omega}_b^2-\omega_0^2\right)b_0\langle\tilde{E}_b|\tilde{E}_b\rangle=\omega_0^2\Gamma_0 D_{\max}\alpha_2\left(a_0\alpha_1+b_0\alpha_2\right)F\left(|\Gamma_0|^2|a_0\alpha_1+b_0\alpha_2|^2\right). \tag{S16}$$

Due to the nonlinear saturation term in the denominator in $P\left(x\right)$, the integral is not a constant but a function of $\{a_0,b_0\}$,

$$F\left(y\right)=\int_{\mathrm{C_{act}}}\frac{\mathrm{Win}\left(x\right)E_\alpha\left(x\right)^2}{1+|E_\alpha\left(x\right)|^2 y}dx, \tag{S17}$$

where $y=|\Gamma_0|^2|a_0\alpha_1+b_0\alpha_2|^2$ and the integral interval $\mathrm{C_{act}}$ is the pumped cavity. Therefore, one only needs to precompute the QNMs $\tilde{E}_{a,b}\left(x\right)$ for $\{\alpha_1,\alpha_2,E_\alpha\left(x\right)\}$ in the integral function,

which is just a standard nonlinear eigenvalue problem. Consequently, Eq. (S15)-(S16) are simply nonlinear equations of $\{a_0, b_0\}$, and thus can be solved using any basic nonlinear root-finding solver, as shown in Fig. S1**h**. The conductivity σ of the right cavity is tuned beyond the first threshold as illustrated in Fig. S2.

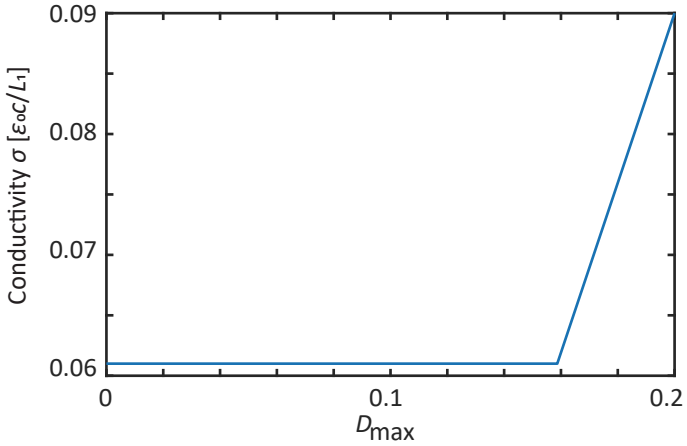

Figure S2: The conductivity σ of the right cavity is tuned above the first threshold to ensure near-EP operation.

The finite electric field of a single-mode lasing solution modifies the spatial distribution of population inversion as the gain saturates, yielding a change in the evolution of nonlasing modes as a function of pump strength. The behavior of the lasing medium operating in the single-mode lasing regime can be understood using a linear stability analysis on the single-mode lasing solution.[S5] Here, we first perform the stability analysis on the single-mode solution, then simplify it using the QNM expansion.

In presence of the single-mode lasing solution $E_0(x)\, e^{-i\omega_0 t}$ defined in Eq. (S13), a perturbation in the electric field with time dependence $e^{-i(\omega_0+\omega_d)t}$ will induce another signal with time dependence $e^{-i\left(\omega_0-\omega_d^*\right)t}$, where ω_d is the complex perturbation frequency. Such a perturbed electric field $\delta E(x,t) = E_1(x)\, e^{-i\omega_1 t} + E_{-1}(x)\, e^{-i\omega_{-1} t}$ is governed by a pair of coupled linear equations,[S5]

$$\frac{d^2E_1(x)}{dx^2}+\left(\frac{\omega_1}{c}\right)^2\varepsilon_r E_1(x)=-\left(\frac{\omega_1}{c}\right)^2\Gamma_+\left[(D_0(x)+\chi_+(x)E_0(x))E_1(x)+\chi_-(x)E_0(x)E_{-1}^*(x)\right], \tag{S18}$$

$$\frac{d^2E_{-1}(x)}{dx^2}+\left(\frac{\omega_{-1}}{c}\right)^2\varepsilon_r E_{-1}(x)=-\left(\frac{\omega_{-1}}{c}\right)^2\Gamma_-\left[(D_0(x)+\chi_-^*(x)E_0(x))E_{-1}(x)+\chi_+^*(x)E_0(x)E_1^*(x)\right], \tag{S19}$$

where $\omega_1=\omega_0+\omega_d$ and $\omega_{-1}=\omega_0-\omega_d^*$. $\Gamma_+=\Gamma_\perp(\omega_1)$ and $\Gamma_-=\Gamma_\perp(\omega_{-1})$ are the dispersive gain factors. $D_0(x)=D_{\mathrm{P}}(x)/\left[1+|\Gamma_\perp(\omega_0)|^2|E_0(x)|^2\right]$ is the saturated population inversion distribution at single-mode lasing operation. The additional two coupling coefficients are determined as

$$\chi_+(x)=\frac{(1/2)\Gamma_\parallel(\Gamma_+-\Gamma_0^*)D_0(x)E_0^*(x)}{1-(1/2)\Gamma_\parallel(\Gamma_+-\Gamma_-^*)|E_0(x)|^2}, \tag{S20}$$

$$\chi_-(x)=\frac{(1/2)\Gamma_\parallel\left(\Gamma_0-\Gamma_-^*\right)D_0(x)E_0(x)}{1-(1/2)\Gamma_\parallel(\Gamma_+-\Gamma_-^*)|E_0(x)|^2}. \tag{S21}$$

Slightly beyond the first lasing threshold D_1^{th}, this nonlinear eigenvalue problem of complex ω_d has solutions with negative imaginary parts, which means the corresponding perturbation would decay exponentially. Therefore, the single-mode lasing solution remains stable.

As the pumping strength $D_{\max}$ increases, the solutions of ω_d moves on the complex plane until one of the solutions reaches the real axis. A real eigenvalue of ω_d indicates a non-decaying perturbation and destabilizes the single-mode lasing solution. This critical point of pumping strength is noted as the comb threshold $D_{\max}=D_c^{th}$.

Under QNM expansion framework, the perturbation fields are also expanded onto the 2-QNM basis: $E_{\pm1}(x)=a_{\pm1}\tilde{E}_a(x)+b_{\pm1}\tilde{E}_b(x)$ and the corresponding nonlinear eigenvalue

problem turns into

$$\left(\tilde{\omega}_a^2-\omega_1^2\right)a_1\langle\tilde{E}_a|\tilde{E}_a\rangle=\omega_1^2\int_{\mathrm{C_{act}}}\tilde{E}_a\left(x\right)\left\{\Gamma_+\left[\left(D_0\left(x\right)+\chi_+\left(x\right)E_0\left(x\right)\right)E_1\left(x\right)+\chi_-\left(x\right)E_0\left(x\right)E_{-1}^*\left(x\right)\right]\right\}dx, \tag{S22}$$

$$\left(\tilde{\omega}_b^2-\omega_1^2\right)b_1\langle\tilde{E}_b|\tilde{E}_b\rangle=\omega_1^2\int_{\mathrm{C_{act}}}\tilde{E}_b\left(x\right)\left\{\Gamma_+\left[\left(D_0\left(x\right)+\chi_+E_0\left(x\right)\right)E_1\left(x\right)+\chi_-\left(x\right)E_0\left(x\right)E_{-1}^*\left(x\right)\right]\right\}dx, \tag{S23}$$

$$\left(\tilde{\omega}_a^2-\omega_{-1}^2\right)a_{-1}\langle\tilde{E}_a|\tilde{E}_a\rangle=\omega_{-1}^2\int_{\mathrm{C_{act}}}\tilde{E}_a\left(x\right)\left\{\Gamma_-\left[\left(D_0\left(x\right)+\chi_-^*\left(x\right)E_0\left(x\right)\right)E_{-1}\left(x\right)+\chi_+^*\left(x\right)E_0\left(x\right)E_1^*\left(x\right)\right]\right\}dx, \tag{S24}$$

$$\left(\tilde{\omega}_b^2-\omega_{-1}^2\right)b_{-1}\langle\tilde{E}_b|\tilde{E}_b\rangle=\omega_{-1}^2\int_{\mathrm{C_{act}}}\tilde{E}_b\left\{\Gamma_-\left[\left(D_0\left(x\right)+\chi_-^*\left(x\right)E_0\left(x\right)\right)E_{-1}\left(x\right)+\chi_+^*\left(x\right)E_0\left(x\right)E_1^*\left(x\right)\right]\right\}dx. \tag{S25}$$

Despite the complicated nonlinear dependence of $E_0\left(x\right)$, Eq. (S22)- (S25) are intrinsically linear equations with respect to variables $\left\{a_1,b_1,a_{-1}^*,b_{-1}^*\right\}$. Therefore, nonzero solution of $\left\{a_1,b_1,a_{-1}^*,b_{-1}^*\right\}$ requires vanishing determinant of the coefficient matrix, leading to complex eigenvalues ω_d.

Noted that the integrals in Eq. (S22)- (S25) are also evaluated only inside $\mathrm{C_{act}}$, the approximation of same field profile inside $\mathrm{C_{act}}$ applies and the linear equations can be simplified as

$$\begin{bmatrix}\omega_1^2\alpha_1I_1\alpha_1 & \omega_1^2\alpha_1I_1\alpha_2 & \omega_1^2\alpha_1I_2\alpha_1^* & \omega_1^2\alpha_1I_2\alpha_2^*\\ \omega_1^2\alpha_2I_1\alpha_1 & \omega_1^2\alpha_2I_1\alpha_2 & \omega_1^2\alpha_2I_2\alpha_1^* & \omega_1^2\alpha_2I_2\alpha_2^*\\ \left(\omega_{-1}^*\right)^2\alpha_1^*I_3^*\alpha_1 & \left(\omega_{-1}^*\right)^2\alpha_1^*I_3^*\alpha_2 & \left(\omega_{-1}^*\right)^2\alpha_1^*I_4^*\alpha_1^* & \left(\omega_{-1}^*\right)^2\alpha_1^*I_4^*\alpha_2^*\\ \left(\omega_{-1}^*\right)^2\alpha_2^*I_3^*\alpha_1 & \left(\omega_{-1}^*\right)^2\alpha_2^*I_3^*\alpha_2 & \left(\omega_{-1}^*\right)^2\alpha_2^*I_4^*\alpha_1^* & \left(\omega_{-1}^*\right)^2\alpha_2^*I_4^*\alpha_2^*\end{bmatrix}\begin{bmatrix}a_1\\b_1\\a_{-1}^*\\b_{-1}^*\end{bmatrix}$$
$$-\mathrm{diag}\begin{bmatrix}\left(\tilde{\omega}_a^2-\omega_1^2\right)\langle\tilde{E}_a|\tilde{E}_a\rangle\\ \left(\tilde{\omega}_b^2-\omega_1^2\right)\langle\tilde{E}_b|\tilde{E}_b\rangle\\ \left(\tilde{\omega}_a^2-\omega_{-1}^2\right)^*\langle\tilde{E}_a|\tilde{E}_a\rangle^*\\ \left(\tilde{\omega}_b^2-\omega_{-1}^2\right)^*\langle\tilde{E}_b|\tilde{E}_b\rangle^*\end{bmatrix}\begin{bmatrix}a_1\\b_1\\a_{-1}^*\\b_{-1}^*\end{bmatrix}=0, \tag{S26}$$

where I_{1-4} consist of some integrals of the single-mode lasing solution $\{a_0, b_0, \omega_0\}$,

$$I_1 = \Gamma_+ D_{\max} \left\{ F\left(|\Gamma_0|^2 |a_0\alpha_1 + b_0\alpha_2|^2\right) \left(-\frac{\Gamma_-^* - \Gamma_0^*}{\Gamma_+ - \Gamma_-^*} + \frac{|\Gamma_0|^2}{|\Gamma_0|^2 + (1/2)\Gamma_\parallel \left(\Gamma_+ - \Gamma_-^*\right)} \frac{\Gamma_+ - \Gamma_0^*}{\Gamma_+ - \Gamma_-^*} \right) \right.$$
$$\left. + F\left[-(1/2)\Gamma_\parallel \left(\Gamma_+ - \Gamma_-^*\right) |a_0\alpha_1 + b_0\alpha_2|^2 \right] \frac{(1/2)\Gamma_\parallel \left(\Gamma_+ - \Gamma_-^*\right)}{|\Gamma_0|^2 + (1/2)\Gamma_\parallel \left(\Gamma_+ - \Gamma_-^*\right)} \frac{\Gamma_+ - \Gamma_0^*}{\Gamma_+ - \Gamma_-^*} \right\}, \tag{S27}$$

$$I_2 = \Gamma_+ D_{\max} \left\{ F\left[-(1/2)\Gamma_\parallel \left(\Gamma_+ - \Gamma_-^*\right) |a_0\alpha_1 + b_0\alpha_2|^2 \right] - F\left(|\Gamma_0|^2 |a_0\alpha_1 + b_0\alpha_2|^2\right) \right\}$$
$$\times \frac{(1/2)\Gamma_\parallel \left(\Gamma_0 - \Gamma_-^*\right)}{|\Gamma_0|^2 + (1/2)\Gamma_\parallel \left(\Gamma_+ - \Gamma_-^*\right)} \frac{a_0\alpha_1 + b_0\alpha_2}{\left(a_0\alpha_1 + b_0\alpha_2\right)^*}, \tag{S28}$$

$$I_3 = \Gamma_- D_{\max} \left\{ F\left[-(1/2)\Gamma_\parallel^* \left(\Gamma_+^* - \Gamma_-\right) |a_0\alpha_1 + b_0\alpha_2|^2 \right] - F\left(|\Gamma_0|^2 |a_0\alpha_1 + b_0\alpha_2|^2\right) \right\}$$
$$\times \frac{(1/2)\Gamma_\parallel^* \left(\Gamma_+^* - \Gamma_0\right)}{|\Gamma_0|^2 + (1/2)\Gamma_\parallel^* \left(\Gamma_+^* - \Gamma_-\right)} \frac{a_0\alpha_1 + b_0\alpha_2}{\left(a_0\alpha_1 + b_0\alpha_2\right)^*}, \tag{S29}$$

$$I_4 = \Gamma_- D_{\max} \left\{ F\left(|\Gamma_0|^2 |a_0\alpha_1 + b_0\alpha_2|^2\right) \left(-\frac{\Gamma_0^* - \Gamma_+^*}{\Gamma_+^* - \Gamma_-} + \frac{|\Gamma_0|^2}{|\Gamma_0|^2 + (1/2)\Gamma_\parallel^* \left(\Gamma_+^* - \Gamma_-\right)} \frac{\Gamma_0^* - \Gamma_-}{\Gamma_+^* - \Gamma_-} \right) \right.$$
$$\left. + F\left[-(1/2)\Gamma_\parallel^* \left(\Gamma_+^* - \Gamma_-\right) |a_0\alpha_1 + b_0\alpha_2|^2 \right] \frac{(1/2)\Gamma_\parallel^* \left(\Gamma_+^* - \Gamma_-\right)}{|\Gamma_0|^2 + (1/2)\Gamma_\parallel^* \left(\Gamma_+^* - \Gamma_-\right)} \frac{\Gamma_0^* - \Gamma_-}{\Gamma_1^* - \Gamma_-}. \right\} \tag{S30}$$

Once the single-mode lasing solution $\{a_0, b_0, \omega_0\}$ is known, I_{1-4} are just integral functions of ω_d, and so is the determinant of the coefficient matrix in Eq. (S26). Typical root-finding methods can be applied to find the zeros of this determinant, which corresponds to the complex perturbation frequency ω_d. By tracing ω_d while increasing $D_{\max}$, the comb threshold D_c^{th} can be found when ω_d reaches the real axis, marked as circles in Fig. S1.

S4: QNM-PALT: frequency comb solution for near EP lasers

In this section, we apply the QNM expansion formalism to the EP comb generation and make an accurate prediction of the EP comb solution.

Above the comb lasing threshold $D_{\max} > D_c^{th}$, the EP comb solution $E(x,t) = \sum_m E_m(x) e^{-i\omega_m t}$ are determined by the PALT equations,[S5]

$$\frac{d^2 E_m(x)}{dx^2} + \frac{\omega_m^2}{c^2}\varepsilon_r(x) E_m(x) = -\frac{\omega_m^2}{c^2}\Gamma_\perp(\omega_m) \sum_{n=-\infty}^{+\infty} D_{m-n}(x) E_n(x), \tag{S31}$$

$$\bar{D}(x) = D_{\mathrm{p}}(x) \left[\bar{\bar{I}} - (1/2)\bar{\bar{\Gamma}}_\parallel \left(\bar{\bar{E}}^\dagger(x)\bar{\bar{\Gamma}}_+ \bar{\bar{E}}(x) - \bar{\bar{E}}(x)\bar{\bar{\Gamma}}_-^\dagger \bar{\bar{E}}^\dagger(x)\right)\right]^{-1} \bar{\delta}, \tag{S32}$$

where $\omega_m = \omega_0 + m\omega_d$ is the frequency of the mth Fourier component $E_m(x)$. The dynamic population inversion is expressed as $D(x,t) = \sum_n D_n(x) e^{-in\omega_d t}$. At equilibrium, the population inversion induced by electric field are determined by Eq. (S32), where $\bar{D}(x)$ and $\bar{\delta}$ are column vectors with components $\left(\bar{D}(x)\right)_m = D_m(x)$ and $\left(\bar{\delta}\right)_m = \delta_{m0}$, δ is the Kronecker delta. $\bar{\bar{E}}(x)$ is the electric field matrix filled with different Fourier components $\left(\bar{\bar{E}}(x)\right)_{mn} = E_{m-n}(x)$. $\bar{\bar{\Gamma}}_\parallel$ and $\bar{\bar{\Gamma}}_\pm$ are diagonal matrices with $\left(\bar{\bar{\Gamma}}_\parallel\right)_{mn} = \delta_{m-n}\gamma_\parallel / \left(m\omega_d + i\gamma_\parallel\right)$ and $\left(\bar{\bar{\Gamma}}_\pm\right)_{mn} = \delta_{m-n}\Gamma_\perp(\omega_{\pm m})$. $\bar{\bar{I}}$ is the identity matrix and † stands for matrix conjugate transpose.

Expanding all of the Fourier components onto the 2-QNM basis, $E_m(x) = a_m \tilde{E}_a(x) + b_m \tilde{E}_b(x)$, the QNM amplitudes $\{a_m, b_m\}$ are determined by

$$\left(\tilde{\omega}_a^2 - \omega_m^2\right) a_m \langle \tilde{E}_a | \tilde{E}_a \rangle = \omega_m^2 \int_{\mathrm{C_{act}}} \tilde{E}_a(x)\Gamma_\perp(\omega_m) \sum_{n=-\infty}^{+\infty} D_{m-n}(x) E_n(x)\, dx, \tag{S33}$$

$$\left(\tilde{\omega}_b^2 - \omega_m^2\right) b_m \langle \tilde{E}_b | \tilde{E}_b \rangle = \omega_m^2 \int_{\mathrm{C_{act}}} \tilde{E}_b(x)\Gamma_\perp(\omega_m) \sum_{n=-\infty}^{+\infty} D_{m-n}(x) E_n(x)\, dx. \tag{S34}$$

For the integral inside $\mathrm{C_{act}}$, we apply the same field profile approximation again and simplify

the integrals as

$$\int_{\mathrm{C_{act}}} \tilde{E}_{a,b}\left(x\right)\Gamma_{\perp}\left(\omega_m\right)\sum_{n=-\infty}^{+\infty} D_{m-n}\left(x\right)E_n\left(x\right)dx \approx D_{\max}\alpha_{1,2}\sum_n M_{m-n}\left(a_n\alpha_1+b_n\alpha_2\right), \quad \text{(S35)}$$

where $M_{m-n}=\bar{M}_{m-n}$ and $\bar{M}$ is a column vector defined as

$$\bar{M}=\bar{\bar{\Gamma}}_{\perp}\int_{\mathrm{C_{act}}}\left[\bar{\bar{I}}+\bar{\bar{I}}_{\mathrm{eff}}|E_{\alpha}\left(x\right)|^2\right]^{-1}\bar{\delta}\mathrm{Win}\left(x\right)E_{\alpha}^2\left(x\right)dx, \quad \text{(S36)}$$

and $\bar{\bar{I}}_{\mathrm{eff}}$ is the effective intensity matrix

$$\bar{\bar{I}}_{\mathrm{eff}}=\frac{1}{2}\bar{\bar{\Gamma}}_{\parallel}\left[\left(\alpha_1\bar{\bar{A}}+\alpha_2\bar{\bar{B}}\right)\bar{\bar{\Gamma}}_{-}^{\dagger}\left(\alpha_1^{*}\bar{\bar{A}}^{\dagger}+\alpha_2^{*}\bar{\bar{B}}^{\dagger}\right)-\left(\alpha_1^{*}\bar{\bar{A}}^{\dagger}+\alpha_2^{*}\bar{\bar{B}}^{\dagger}\right)\bar{\bar{\Gamma}}_{+}\left(\alpha_1\bar{\bar{A}}+\alpha_2\bar{\bar{B}}\right)\right], \quad \text{(S37)}$$

and $\bar{\bar{A}}$, $\bar{\bar{B}}$ are the amplitude matrices $\left(\bar{\bar{A}}\right)_{mn}=a_{m-n}$ and $\left(\bar{\bar{B}}\right)_{mn}=b_{m-n}$. The vectorial integral in Eq. (S36) is integrated for each element separately.

Equations (S33)-(S34) are nonlinear integral equations of variables $\{a_m, b_m, \omega_0, \omega_d\}$ and are generally solvable with the well-developed root-finding techniques. However, the presence of Eq. (S36) poses a great challenge in practical numerical computation due to repetitious evaluation of the matrix inverse at each position x and the subsequent integral for all matrix elements.

To simplify this numerical problem, we recognize that the effective intensity matrix Eq. (S37) is independent of space, thus can be diagonlized as space-independent eigenvalues and eigenvectors, $\bar{\bar{I}}_{\mathrm{eff}}=\bar{\bar{P}}^{-1}\bar{\bar{\Lambda}}\bar{\bar{P}}$. Substituting back into Eq. (S36), we obtain

$$\begin{aligned}\bar{M}&=\bar{\bar{\Gamma}}_{\perp}\bar{\bar{P}}^{-1}\left\{\int_{\mathrm{C_{act}}}\left[\bar{\bar{I}}+\bar{\bar{\Lambda}}|E_{\alpha}\left(x\right)|^2\right]^{-1}\mathrm{Win}\left(x\right)E_{\alpha}^2\left(x\right)dx\right\}\bar{\bar{P}}\bar{\delta}\\&=\bar{\bar{\Gamma}}_{\perp}\bar{\bar{P}}^{-1}\bar{\bar{F}}\left(\bar{\bar{\Lambda}}\right)\bar{\bar{P}}\bar{\delta},\end{aligned} \quad \text{(S38)}$$

where $\bar{\bar{F}}\left(\bar{\bar{\Lambda}}\right)$ is a matrix generalization of the scalar function $\left[\bar{\bar{F}}\left(\bar{\bar{\Lambda}}\right)\right]_{m,n}=F\left[\left(\bar{\bar{\Lambda}}\right)_{m,n}\right]$. Compared with the original expression in Eq. (S36), the space-independent matrix diagonal-

ization in Eq. (S38) is performed only once and the integral is computed only for the diagonal elements, while the space-dependent matrix inverse should be performed everywhere inside the integral interval C_{act} and the integral is computed for every element in the matrix.

S5: Padé approximant

Although the repetitive matrix inverse in Eq. (S36) is bypassed by a diagonalization approach in Eq. (S38), the evaluation of the integral function $F(y)$ in Eq. (S17) can be the bottleneck of a computation. In particular, the finite-difference simulation of this EP comb needs an abnormally small spatial grid size for convergence,[S5] which makes the integral computation even slower. Here we propose a numerical trick, which is a rational expansion of the integral function, to approximate the integral efficiently.

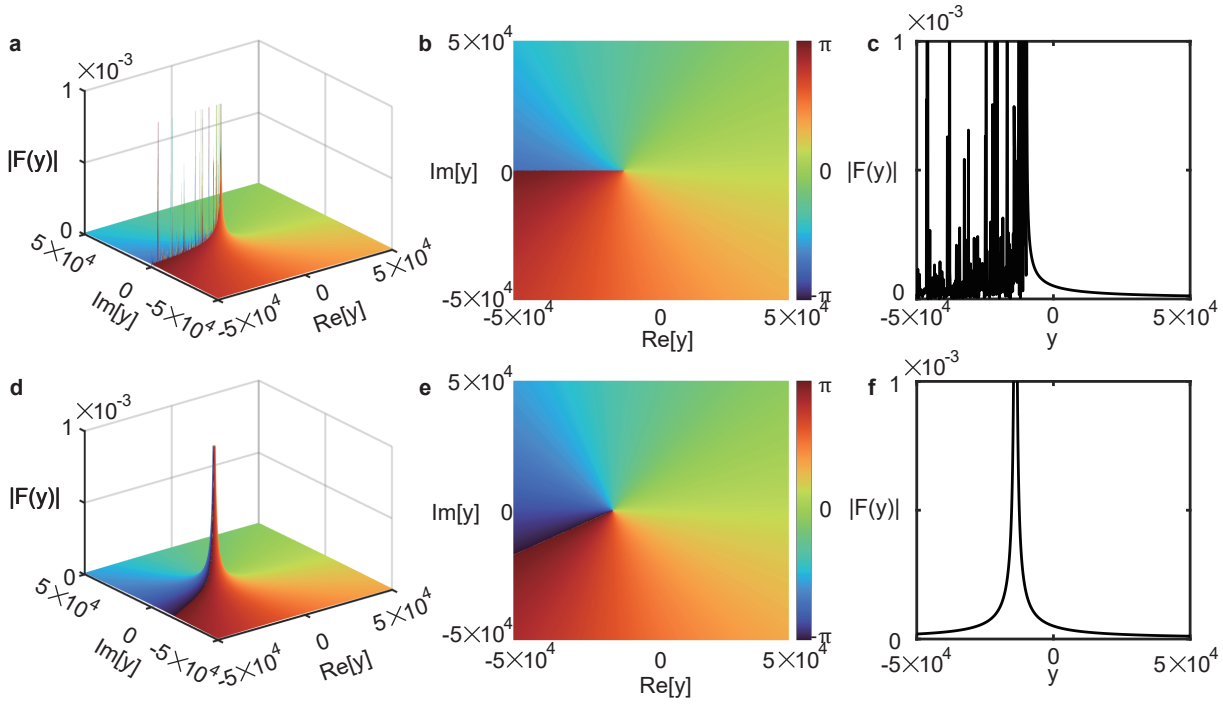

Figure S3: **a**, **d** Absolute value of $F(y)$ on the complex y plane. **b**, **e** Phase of $F(y)$ on the complex y plane. **c**, **f** Absolute value of $F(y)$ with real variable y. The first row are evaluated through the original integral function while the second row are evaluated as its Padé approximant. The uneven singular behavior in **a-c** is because of the finite sampling rate in the discretized electric field $E_\alpha(x_i)$.

From the definition in Eq.(S17), $F(y)$ is analytic on the entire complex y plane, except for a branch cut on the real axis $y = -1/|E_\alpha(x)|^2$, where $x \in \mathrm{C_{act}}$. As illustrated in Fig. S3 **a**-**c**, $F(y)$ is a smooth function across the complex y plane with divergent behavior on part of the real axis. In Fig. S3 **a** & **c** the non-analyticity seems discrete due to the discrete finite-difference data of $E_\alpha(x)$, and it should be continuous in general.

In the general context of nonlinear optics, the nonlinearity is always small and treated as perturbation.[S6] Therefore, a Taylor series expansion of the nonlinearity can be adopted, leading to the well known $\chi^{(2)}$, $\chi^{(3)}$, and higher order $\chi^{(n)}$ effects. However, the nonlinearity in laser medium originates mainly from the mode competition caused by gain saturation, which could deprive most of the gain and leave very little gain for the rest modes when operating at high intensities. Such vanishing behavior of $F(y)$ at infinity intensity falls outside the radius of convergence of Taylor expansion thus cannot be captured by a Taylor series expansion in general.

Instead of a Taylor series expansion, here we use a rational function expansion

$$F(y) = \int_{\mathrm{C_{act}}} \frac{\mathrm{Win}(x) E_\alpha(x)^2}{1 + |E_\alpha(x)|^2 y} dx \approx \frac{P(y)}{Q(y)} \tag{S39}$$

to estimate the function value. $P(y)$, $Q(y)$ are polynomial function of y. Such estimation is also referred to as the Padé approximant of $F(y)$.[S7,S8] We find that the the simplest form of $F(y) \approx \frac{\lambda}{1+\mu y}$ is sufficient to provide a rather good estimate of $F(y)$. $\{\lambda, \mu\}$ are complex constants and can be fitted from some precomputation. For instance, one can evaluate $F(y)$ for real valued y then fit the result with $F(y) \approx \frac{\lambda}{1+\mu y}$, as illustrated in Fig. 3**a**-**b** in the main text.

As shown in Fig. S3**d**-**f**, the new rational function $F(y) \approx \frac{\lambda}{1+\mu y}$ only has one single pole $y = -1/\mu$ around the negative real axis, which serves as a weighted average over all the poles of original $F(y)$. The error distribution of this estimation is plotted as contour lines on the complex y plane in Fig. S4. An accuracy of 10% is achieved for most regions with a

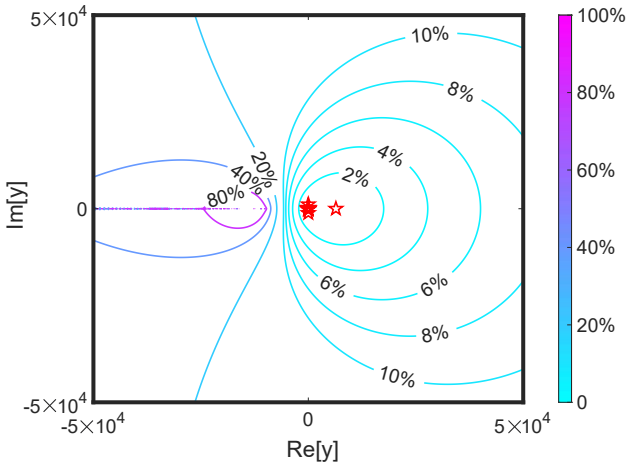

Figure S4: The error distribution of a Padé approximant in $F(y)$ evaluation on the complex y plane. The error is defined as the relative difference between the approximant and the exact value: error $= |\left(F_{\text{approximant}} - F_{\text{original}}\right)/F_{\text{original}}|$. The red pentagrams marks the variables of $F\left(y\right)$ in the comb solution shown in Fig. 4**f**.

positive real part. Moreover, the practical complex variable y in laser operations resides near the positive real axis, which leads to much higher accuracy. For instance, in the single-mode lasing operation, $y = |\Gamma_0|^2|a_0\alpha_1 + b_0\alpha_2|^2$ is real, this yielding high accuracy. For the EP comb solution, the values of y, which are the eigenvalues of the effective intensity matrix $\bar{\bar{I}}_{\text{eff}}$, are plotted as red pentagrams in Fig. S4. All of these eigenvalues are enclosed by the contour line of 2% relative error. Such a low level of error ensures a good estimation of $F\left(y\right)$, leading to an accurate and efficient way to evaluate the integral function and perform PALT-related computations.

S6: 1D FDTD simulation of MB equations

In this section, we present the numerical challenges in FDTD simulation of MB equations.

The intrinsic high sensitivity of EP also amplifies numerical error, requiring an unusually high precision when using FDTD to capture intricate laser dynamics in MB equations. Fig. S5 **a** and **b** shows the result of an FDTD simulation with 20 pixels per wavelength in medium, which is enough for typical FDTD simulations. Such FDTD simulation converges to a single-mode lasing solution, which should be unstable at this pumping strength

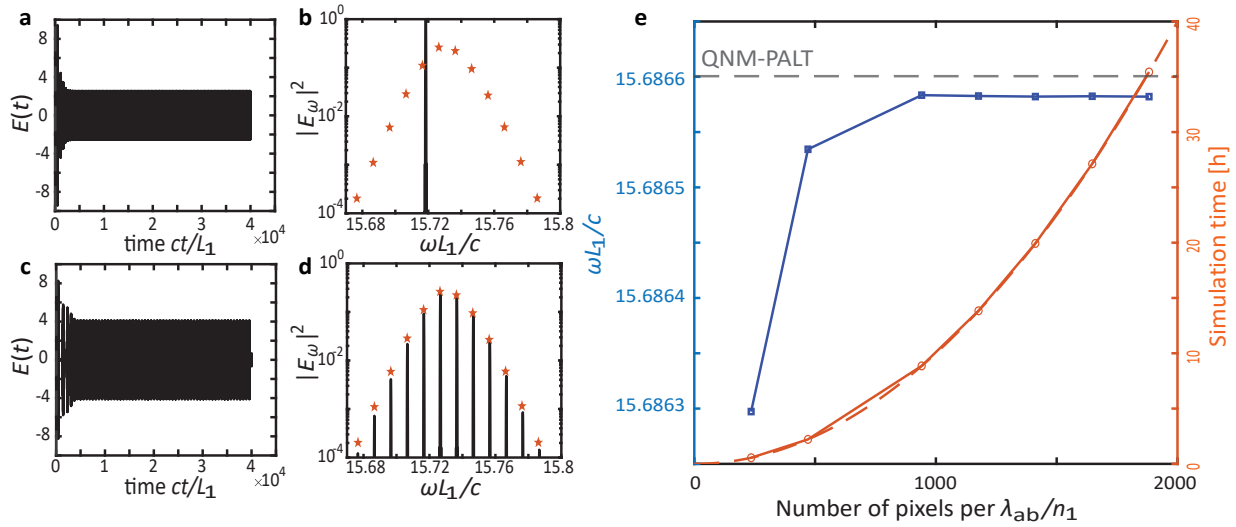

Figure S5: MB equations FDTD simulation of the EP comb presented in Fig. 4**ef**. **a**, **c** Time domain data of electric field at a fixed point with a resolution of 20 and 200 pixels per wavelength in medium. **b**, **d** The black solid curve is the spectrum of the time series data in **a** and **c**. The red pentagrams in **b** and **d** represent the comb spectrum predicted by QNM-PALT. **e** The convergence trend of one comb line frequency and simulation time as a function of number of pixels per wavelength in medium. The gray dashed line marks the frequency calculated from QNM-PALT.

as predicted by stability analysis. As we increase the discretization resolution from 20 to 200 pixels per wavelength in medium, the FDTD simulation converges to a clear comb solution, showing great agreement with respect to the QNM-PALT result. From Fig. S5 **e**, one can conclude that MB equations FDTD simulation of EP comb typically requires a small discretization error for convergence, thus an extremely long simulation time is inevitable. Since the simulation time of FDTD scales with respect to the total number of pixels, quadratically for 1D, cubically for 2D, and quartically for 3D, the simulation in 2D and 3D structures with a small discretization error is obviously unscalable.

S7: QNM-PALT for a 2D coupled-disk resonator system

In this section, we present the application of the QNM-PALT framework to the 2D coupled-disk system illustrated in Fig. 5.

Fig. S6 **a** shows the trajectory of the complex eigenfrequencies under linear gain, manifesting typical near-EP behavior. Both the two frequencies begin with low loss QNMs when no pumping applied, then move toward the real axis until mode b reaches the real axis, marking the first lasing threshold. Beyond the first lasing threshold, the gain saturates and leads to stable single-mode lasing action, as illustrated in Fig. S6 **b**. Meanwhile, the stability analysis of the single-mode lasing solution predicts two complex frequencies stemming from the original two QNMs under the real axis, plotted as a function of the pumping strength $D_{\max}$ in Fig. S6 **c**. As $D_{\max}$ further increases, one of the two frequencies reaches real axis, corresponding to the comb threshold. Beyond the comb threshold, one can obtain the comb spectrum Fig. S6 **d** by solving the purely algebraic QNM-PALT equations directly.

References

(S1) Yan, W.; Faggiani, R.; Lalanne, P. Rigorous modal analysis of plasmonic nanoresonators. *Physical Review B* **2018**, *97*, 205422.

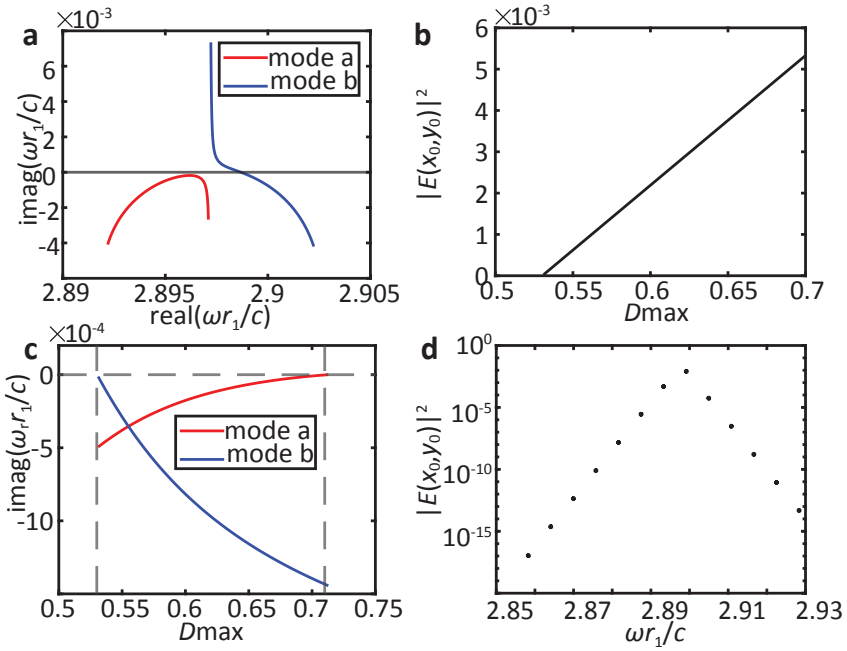

Figure S6: MB equations FDTD simulation of the EP comb presented in Fig. 4**ef**. **a**, **c** Time domain data of electric field at a fixed point with a resolution of 20 and 200 pixels per wavelength in medium. **b**, **d** The black solid curve is the spectrum of the time series data in **a** and **c**. The red pentagrams in **b** and **d** represent the comb spectrum predicted by QNM-PALT. **e** The convergence trend of one comb line frequency and simulation time as a function of number of pixels per wavelength in medium. The gray dashed line marks the frequency calculated from QNM-PALT.

(S2) Sauvan, C.; Hugonin, J.-P.; Maksymov, I. S.; Lalanne, P. Theory of the spontaneous optical emission of nanosize photonic and plasmon resonators. *Physical Review Letters* **2013**, *110*, 237401.

(S3) Lalanne, P.; Yan, W.; Vynck, K.; Sauvan, C.; Hugonin, J.-P. Light interaction with photonic and plasmonic resonances. *Laser & Photonics Reviews* **2018**, *12*, 1700113.

(S4) Gigli, C.; Wu, T.; Marino, G.; Borne, A.; Leo, G.; Lalanne, P. Quasinormal-mode non-hermitian modeling and design in nonlinear nano-optics. *ACS photonics* **2020**, *7*, 1197–1205.

(S5) Gao, X.; He, H.; Sobolewski, S.; Cerjan, A.; Hsu, C. W. Dynamic gain and frequency comb formation in exceptional-point lasers. *Nature Communications* **2024**, *15*, 8618.

(S6) Boyd, R. W.; Gaeta, A. L.; Giese, E. *Springer Handbook of Atomic, Molecular, and Optical Physics*; Springer, 2008; pp 1097–1110.

(S7) Baker Jr, G. A.; Gammel, J. L. The padé approximant. *Journal of Mathematical Analysis and Applications* **1961**, *2*, 21–30.

(S8) Baker Jr, G. A. *The theory and application of the Padé approximant method*; 1964.